Induced polarization as a tool to characterize shallow landslides

A Revil, A Soueid Ahmed, A Coperey, Ludovic Ravanel, R Sharma, N Panwar

Journal of Hydrology 589 (2020) 125369

Contents lists available at ScienceDirect

Journal of Hydrology

journal homepage: www.elsevier.com/locate/jhydrol

Research papers

Induced polarization as a tool to characterize shallow landslides

A. Revil[a,*], A. Soueid Ahmed[a], A. Coperey[a], L. Ravanel[a], R. Sharma[b], N. Panwar[b]

[a] Univ. Grenoble Alpes, Univ. Savoie Mont-Blanc, CNRS, UMR CNRS 5204, EDYTEM, 73370 Le Bourget du Lac, France
[b] Roorkee University, India

ARTICLE INFO

This manuscript was handled by Jiri Simunek, Editor-in-Chief

Keywords:
Induced polarization
Landslides
Flow path
Permeability

ABSTRACT

The development of shallow landslides is strongly connected to the changes in the water content of soils on hillslopes, their clay content and permeability distribution, which, in turn, are playing an important role regarding their hydro-mechanical properties. A non-intrusive geophysical method able to map these properties would be very helpful. The most common geoelectrical method, DC (Direct Current) resistivity, cannot be used as a stand-alone technique for this purpose since it depends on two contributions (bulk and surface conductivities), which depend on the water content and the cation exchange capacity (CEC) of the material. Induced polarization is a geophysical method that can be now used to complement DC resistivity in providing key material properties that can be used to diagnose potential risks for failure. We first recall the basic principles behind the induced polarization method from laboratory to field scales and key findings in the underlying petrophysics needed to jointly interpret electrical conductivity and normalized chargeability tomograms. Then, we apply these relationships to a field survey carried out over a shallow landslide at Claix (Isère, France), close to Grenoble. A 3D induced polarization survey was carried out and interpreted in terms of the clay content, water content, and permeability distributions. We demonstrate that the landslide is associated with a channel of high water content corresponding with the presence of travertine, a flow-path, and a permeability barrier downslope corresponding to the presence of plastic clays. This study demonstrates that induced polarization can be used to characterize the impacted volume and therefore might have been useful to map the area before the landslide to assess the possible risk of failure. This methodology could play a key role in mitigation planning.

1. Introduction

Because of the threat that landslides pose to public safety, research aims at better understanding slope stability and failure processes while climate change is currently generating more and more extreme rainfall events (Alpert et al., 2002; Maraun et al., 2010), which, in turn, may trigger more shallow landslides, earthflows, and geohazards (e.g., Malet et al., 2007; Samyn et al., 2012; Brückl et al., 2013). These shallow landslides and earthflows increase risks on human housing, infrastructures, and are responsible for casualties around the globe (e.g., Salvati et al., 2018; Sultana, 2020). One of the most important processes triggering landslides relates to the hydro-mechanical behavior of shallow Earth material with drastic changes in their water content and fluid pressure associated with sudden and strong rainfalls (Take et al., 2004; Lourenço et al., 2006; Oh and Lu, 2015; Yang et al., 2019). A 3D (and even a 4D) characterization of the material properties of areas prone to landslides is therefore critical to model such geohazards associated with preferential groundwater flow paths and the occurrence of clay-rich areas acting as permeability barriers (Lu and Godt, 2013).

Drilling and trenching are the classical techniques used to characterize areas prone to landslides (Götz and Zimmermann, 1993; Loew et al., 2012). They may be expensive, time-consuming, and bring only local information. Geophysical methods offer a complementary way to non-intrusively characterize and probe the subsurface to better map material properties and their evolution in time (Binley et al., 2015). They have been applied to landslides and earthflows by various researchers (e.g., Schmutz et al., 2000, 2009; Hibert et al., 2012; Malehmir et al., 2013). In the realm of hydrogeophysics, self-potential and induced polarization are two geophysical methods offering useful information to characterize ground water flow (e.g., Soueid Ahmed et al., 2020a), water and clay contents (Soueid Ahmed et al., 2020b), and permeability (Titov et al., 2010; Revil and Florsch, 2010; Soueid Ahmed et al., 2014; Weller et al., 2015), all essential ingredients to better understand and prevent landslides. Induced polarization refers to the study of both conductivity and low-frequency polarization properties of rocks. Electrical conductivity characterizes the ability of rocks to conduct an electrical current for an applied electrical field. Normalized chargeability denotes the ability of porous materials to store reversibly

* Corresponding author.
E-mail addresses: andre.revil@univ-smb.fr (A. Revil), ravi.sharma@es.iitr.ac.in (R. Sharma), npanwar@es.iitr.ac.in (N. Panwar).

https://doi.org/10.1016/j.jhydrol.2020.125369
Received 15 June 2020; Received in revised form 28 July 2020; Accepted 29 July 2020
Available online 02 August 2020
0022-1694/

electrical charges in an applied electrical field generating polarization phenomena that are non-dielectric in nature and observable at low frequencies (below 100 Hertz, Vinegar and Waxman, 1984).

Induced polarization has already been used to characterize landslides (Marescot et al., 2008; Sastry and Mondal, 2012) but only in a very qualitative way and only in sparse studies. With the recent development of petrophysical models able to explain all aspects of induced polarization (Revil et al., 2017a,b,c) and based on a mechanistic understanding of the underlying physico-chemistry, induced polarization has become a powerful quantitative method useable in the field to characterize landslides and their environments.

For the first time, we present a quantitative investigation of induced polarization phenomena to a shallow landslide in the French Alps. The present case study corresponds to the case of Claix, an area already known for its rock slope movements (Bertran, 2003), which was responsible for a death in 2017. We discuss both laboratory and field experiments and the need for a good petrophysical understanding of what is measured in the field to advance the physical interpretation of the electrical conductivity and normalized chargeability tomograms in terms of petrophysical properties.

2. Test site

The test site is used in this study is located in the vicinity of Claix, a few kilometers south of Grenoble, Isère (French Alps). More precisely, it is located on a woody slope bordering the road of Jayères. This is an area characterized by the presence of clay lens overlying the bedrock and the presence of highly porous and mechanically weak travertins. The bedrock is formed by limestones and weathered limestones outcrop in various areas of the test site. The depth of the top of the carbonate bedrock formation lies between 0 and 20 m. A high number (> 10) of springs of karstic origin can be observed in the area. These springs are rich in dissolved carbonate. These springs are also responsible for the formation of travertin-type porous crusting. On December 30, 2017, a shallow landslide occurred over an area of 30×17 m^2 (Fig. 1). It mobilized roughly 1000 to 1500 m^3 of earth material killing one person in a house downslope that was partly destroyed by the landslide. The landslide occurred after ten days of rain, associated with significant variations in temperature which could allow snowfall as well as the melting of the snowpack. In order to better understand why the landslide occurred in this area, a geophysical campaign was undertaken in June 2018 using induced polarization and DC resistivity. Four samples were collected at different outcrops to characterize the electrical properties of the lithological end-members. An additional sample of a clean limestone (not from the test site) was added to this collection to represent the unweathered bedrock.

3. Induced polarization: From the laboratory to the field scale

3.1. Spectral induced polarization

In this section, we first describe the theoretical background associated with induced polarization of porous materials. A sketch of the polarization of the electrical double layer is shown in Fig. 2. The electrical conductivity and polarization of a porous material can be characterized by an amplitude $|\sigma|$ (in S m^{-1}, obtained using Ohm's law) and a phase (shift) φ (in rad) between an injected harmonic current and its associated electrical field. We define the complex-valued conductivity $\sigma^*(\omega)$ as:

$$\sigma^*(\omega) = |\sigma| e^{i\varphi} = \sigma'(\omega) + i\sigma''(\omega) \quad (1)$$

where $i^2 = -1$, σ' and σ'' (both in S m^{-1}) denote the in-phase and quadrature conductivity, respectively. The complex conductivity is introduced to separate the effect of conduction (real part) from the effect of polarization (imaginary part). The dynamic Stern layer model developed by Revil et al. (2017a,b,c) represents a key concept developed to understand and rationalize the underlying physics of induced polarization. According to this model, the complex conductivity is given by

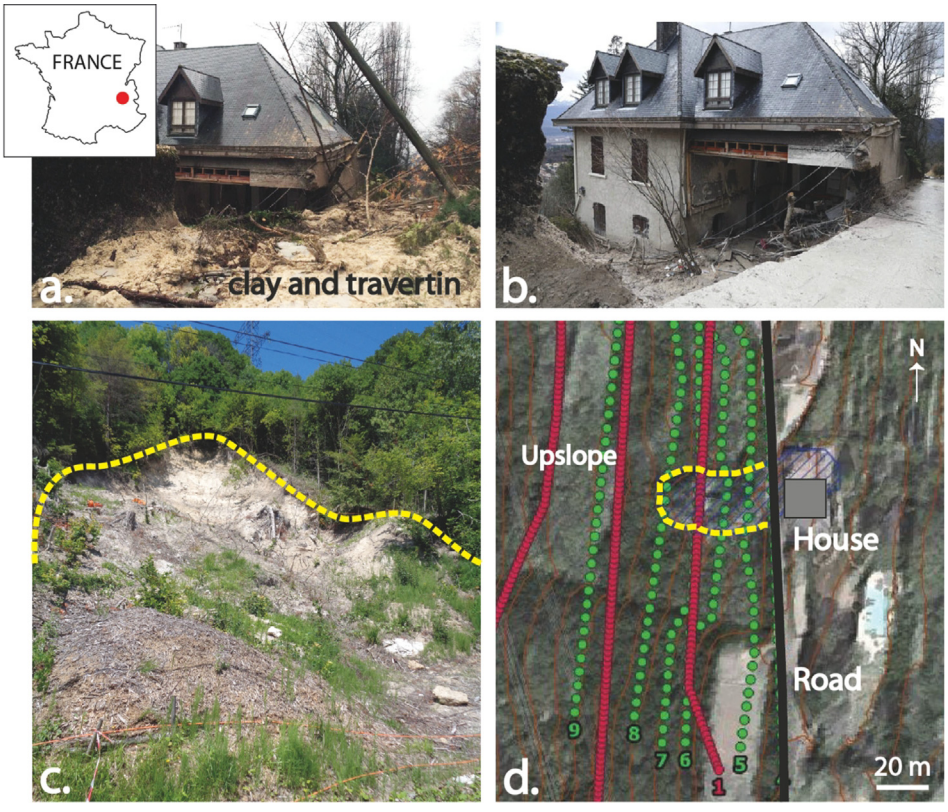

Fig. 1. The shallow landslide of Claix (Isère, France) of December 30, 2017. **a**. Clayey and travertine-type materials have crossed the road and partly destroyed a house killing a person during the night (ph. G. Guais; December 30, 2017). **b**. State of the building after clearing of the mud (ph.: S. Gominet – IRMa; January 03, 2018). **c**. Detachment scar of the landslide on the June 19, 2018. Yellow dotted line: scar border. In the foreground: cables and electrodes. **d**. Geophysical profiles and location of the landslide. The dots correspond to the electrodes.

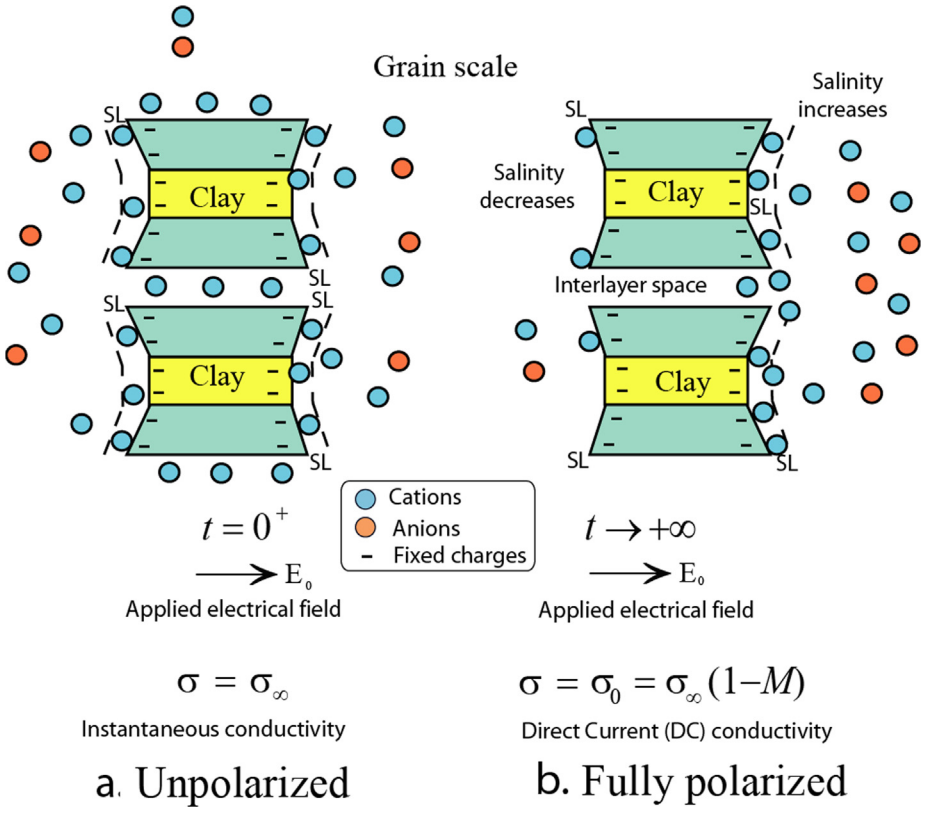

Fig. 2. Polarization of the electrical double layer around a grain associated with the application of an external (applied) electrical field. **a.** Unpolarized clay grain just at the time of the application of the electrical field. This states defines the instantaneous electrical field. **b.** Fully polarized grain for a long application of the electrical field (DC, Direct Current, condition). The quantities σ_∞, σ_0, and M define the instantaneous conductivity, the DC conductivity, and the chargeability, respectively.

$$\sigma*(\omega) = \sigma_\infty - M_n \int_0^\infty \frac{h(\tau)}{1+(i\omega\tau)^{1/2}} d\tau + i\omega\varepsilon_\infty \quad (2)$$

$$\sigma_\infty = \theta^m \sigma_w + \theta^{m-1}\rho_g B\,\mathrm{CEC} \quad (3)$$

$$\sigma_0 = \theta^m \sigma_w + \theta^{m-1}\rho_g (B-\lambda) CEC \quad (4)$$

$$M_n = \theta^{m-1}\rho_g \lambda\,\mathrm{CEC} \quad (5)$$

where τ is a relaxation time (in s), and $h(\tau)$ denotes a (normalized) probability density for the relaxation times of the soil, and ε_∞ denotes the permittivity of the material (in F m^{-1}). The last term of equation (2) will not be used in this study. The quantity σ_∞ (S m^{-1}) defines the instantaneous conductivity of the material (Fig. 2) while σ_0 (S m^{-1}) corresponds to the DC (Direct Current) conductivity of the material (Fig. 2). The normalized chargeability M_n corresponds to the difference between the instantaneous conductivity and the DC conductivity $M_n \equiv \sigma_\infty - \sigma_0$. In Eqs. (3)–(5), θ (dimensionless) denotes the (volumetric) water content, ρ_g denotes the grain density (in kg m^{-3}), and CEC denotes the cation exchange capacity of the material expressed in C kg^{-1} or in meq/100 g (1 meq/100 g = 963.20C kg^{-1}), B(Na$^+$, 25 °C) = 3.1 ± 0.3 × 10^{-9} m^{-2}s^{-1}V^{-1} denotes the apparent mobility of the counterions for surface conduction (associated with the in-phase conductivity) and λ(Na$^+$, 25 °C) = 3.0 ± 0.7 × 10^{-10} m^{-2}s^{-1}V^{-1}, (in m^{2}s^{-1}V^{-1}) denotes the apparent mobility of the counterions for the polarization associated with the quadrature conductivity (see Vinegar and Waxman, 1984). A dimensionless number R was introduced by Revil et al. (2017a,b,c) as $R = \lambda/B \approx 0.10 \pm 0.02$.

Considering the quadrature conductivity at the geometric mean frequency of two frequencies f_1 and f_2 and the normalized chargeability defined as the difference between the in-phase conductivity at the frequency $f_2 (> f_1)$ and the in-phase conductivity at the lower frequency f_1, we can connect the quadrature conductivity and the normalized chargeability with (Revil et al., 2017a)

$$\sigma''(\sqrt{f_1 f_2}) \approx -\frac{M_n(f_1, f_2)}{\alpha} \quad (6)$$

and $\alpha \approx (2/\pi)\ln A$, where A is the number of decades between f_1 andf_2. For instance, for 3 decades $A = 10^3$ and $\alpha \approx 4.4$. From Eq. (6) and the expression of the surface conductivity (the last term of Eq. (3)), we can draw a relationship between the quadrature conductivity and the surface conductivity as $-\sigma''/\sigma \to M_n/\alpha\sigma_S = R/\alpha \approx 0.01$.

According to Soueid Ahmed et al. (2020b), the permeability can be determined as:

$$k \approx \frac{k_0 \theta^6}{(\rho_g CEC)^2} \quad (7)$$

with $k_0 = 10^{4.30}$ and k is expressed in m^2. So the permeability can be determined from the water content θ and the CEC. Since the CEC can be related to the pore size, Eq. (7) can be considered as an extension of the Kozeny Carman equation (Revil and Cathles, 1999).

Equations (1)–(7) constitute a good conceptual model but the coefficients for the various parameters would vary from site to site. This is why a petrophysical study is recommended. These set of equations can be however used to bridge the lithology to the electrical parameters of interest in hydrogeophysics.

3.2. Time-domain induced polarization

We discuss now how time-domain induced polarization measurements are performed. This is important to connect the field data (collected through this approach) and the laboratory data for which we use spectral (frequency-domain) induced polarization. In time-domain induced polarization, a box current of a period T is injected in the ground through two current electrodes A and B (Figs. 3 and 4, see for instance Titov et al., 2002). The voltage difference is measured at two voltage electrodes M and N over time during and after the injection and the shut-down of the current, respectively. The apparent (partial) chargeability can be computed as a function of the decaying voltage generated

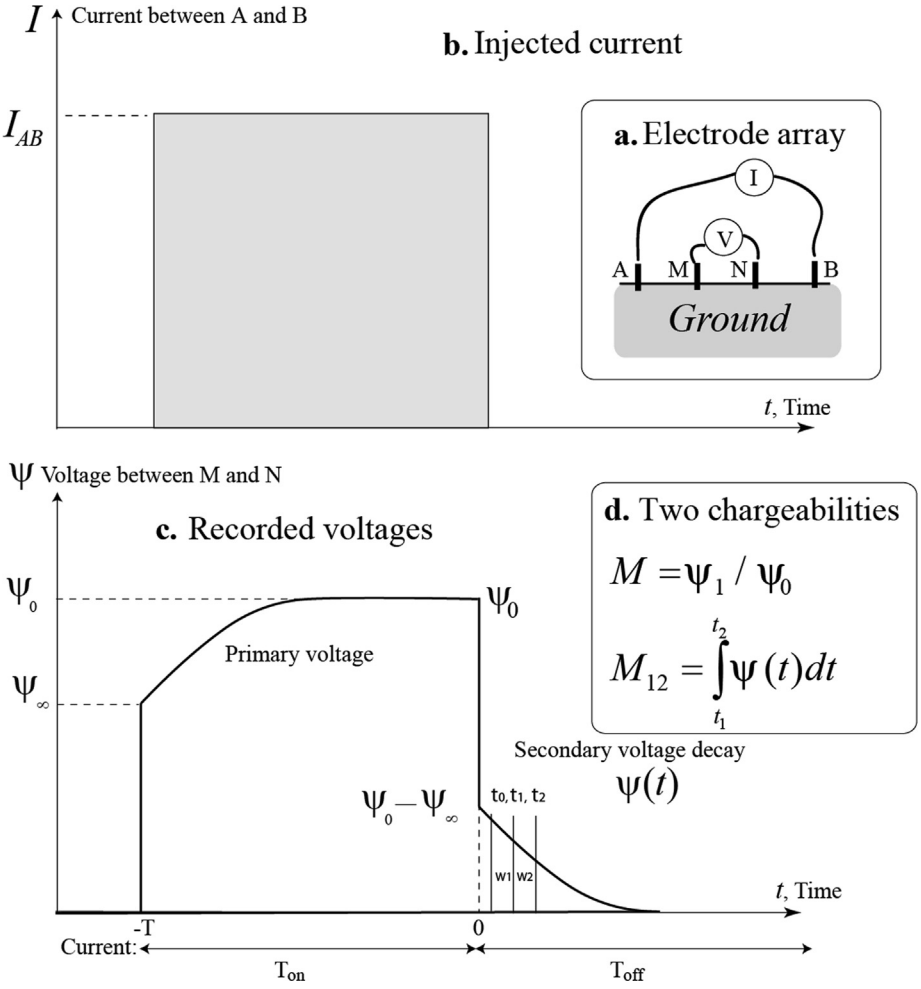

Fig. 3. Induced polarization sequence in the time domain. **a.** Electrode array composed of two current electrodes A and B connected to a current generator. Electrodes M and N are the voltage electrodes connected to a voltmeter characterized by a very high input impedance (typically 100 MOhm). **b.** Box current characterized by a period T_{on}. The duration between two current injection, *Toff*, should be large enough to allow a full decay of the secondary voltage otherwise the potential would build up in the ground for each stack. **c**. Recorded voltage difference between the electrodes M and N. The buildup of the voltage and the decay of the secondary voltage are symmetrical. We distinguish an initial voltage buildup ψ_∞ defining the instantaneous conductivity σ_∞ and a steady-state or direct current (DC) voltage buildup ψ_0 defining the DC conductivity σ_0. **d**. Two chargeabilities can be defined. A total chargeability M (dimensionless) is defined as the difference between the DC potential and the instantaneous potential divided by the Dc potential. In addition, a partial chargeability M_{12} (in s) is defined for a given time window during the decay of the secondary voltage.

after the current shutdown as:

$$M_a = \frac{1}{\delta\psi_0}\int_{t_i}^{t_{i+1}} \delta\psi_{MN}(t)dt \tag{8}$$

where $\delta\psi_{MN}(t)$ is the time dependent decaying voltage recorded between electrodes M and N, ψ_0 is the potential difference between the electrodes M and N recorded just before the shutdown of the primary current, t_i and t_{i+1} are the limits of the window W_i used for recording the secondary voltage ($t_{i+1} - t_i = 100\,ms$ in our case), and t denotes time (see Figs. 3 and 4).

Numerically, we can simulate the apparent chargeability signal by the means of a forward modelling code (in our case using the finite element method) solving for the associated elliptic equation with the appropriate boundary conditions. The electric potential is the solution of the following elliptic partial differential equation governing the forward model

$$-\nabla\cdot(\sigma\nabla\psi) = \Im \tag{9}$$

where $\sigma(\mathrm{Sm}^{-1})$ denotes the electrical conductivity of the medium, ψ (V) is the electrical potential and $\Im$ represents a volumetric source current term (A m^{-3}). This source/sink term is given by the current injected at a given set of electrodes (positive for injection and negative for current retrieval) times the delta function localizing the electrodes and using the superposition principle. The boundary condition at the ground surface is an insulating boundary condition while the potential vanished to zero in the ground far from the source/sink current electrodes. The conductivity is in between an instantaneous value σ_∞ and a steady-state (DC) value $\sigma_0 (\leqslant \sigma_\infty)$.

Equation (9) is used to compute the forward response of the medium (i.e., resistance and apparent chargeability) as follows:

$$R_a = \frac{\Delta\psi}{I} \tag{10}$$

$$M_a = \frac{\Psi(\sigma(1-M)) - \Psi(\sigma)}{\Psi(\sigma(1-M))} \tag{11}$$

where R_a (in Ohm) is the (apparent) resistance, $\Delta\psi$ (in V) is the electrical potential difference between two voltage electrodes M and N (Figs. 3 and 4), and Ma(−) denotes the apparent chargeability (dimensionless but often expressed in mV/V), Ψ defines the forward operator given by Eq. (9) and M (dimensionless) denotes the intrinsic chargeability of the medium. Equation (11) is of high convenience, because it stipulates that computing the apparent chargeability does not require a new equation beside the one involved for the widely used electrical resistivity tomography. For taking into account the polarization effects of the medium, we only need to solve the electrical potential elliptic equation twice.

3.3. A strategy to interpret the field data

From Eqs. (3) and (5), we can get the distribution of the CEC and water content from the normalized chargeability and the (instantaneous) conductivity according to

$$CEC = \frac{M_n}{\theta^{m-1}\rho_g\lambda} \tag{12}$$

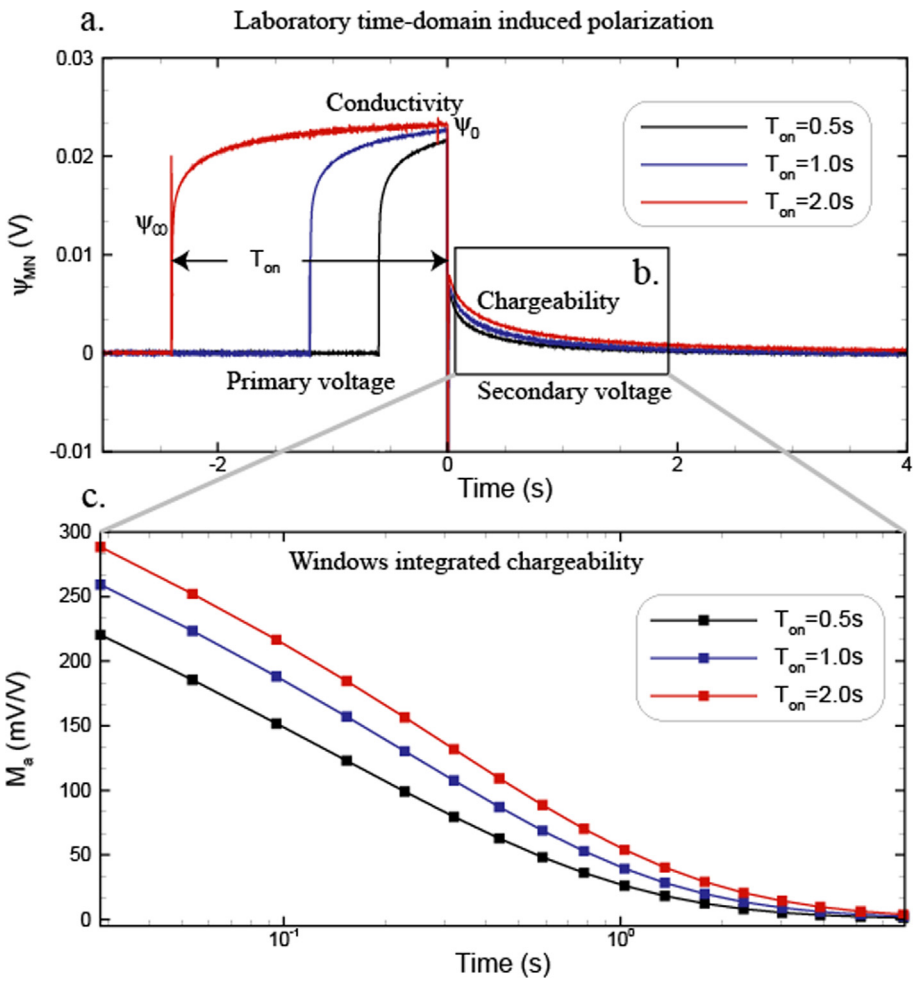

Fig. 4. Example of time-domain induced polarization measurements for three durations of the current injection. **a.** Difference of potential recorded between two electrodes M and N. The current is injected between two electrodes A and B for the time T_{on}. The voltage differences ψ_0 and ψ_∞ correspond to the DC and instantaneous voltages used to define the DC (Direct Current) and instantaneous conductivities, respectively. **b.** Secondary voltage decay used to determine to determine the apparent chargeabilities. **c.** Time window integrated (apparent) chargeability for 17 time-windows. T_{on} corresponds to the period (duration) of the current injection between electrodes A and B.

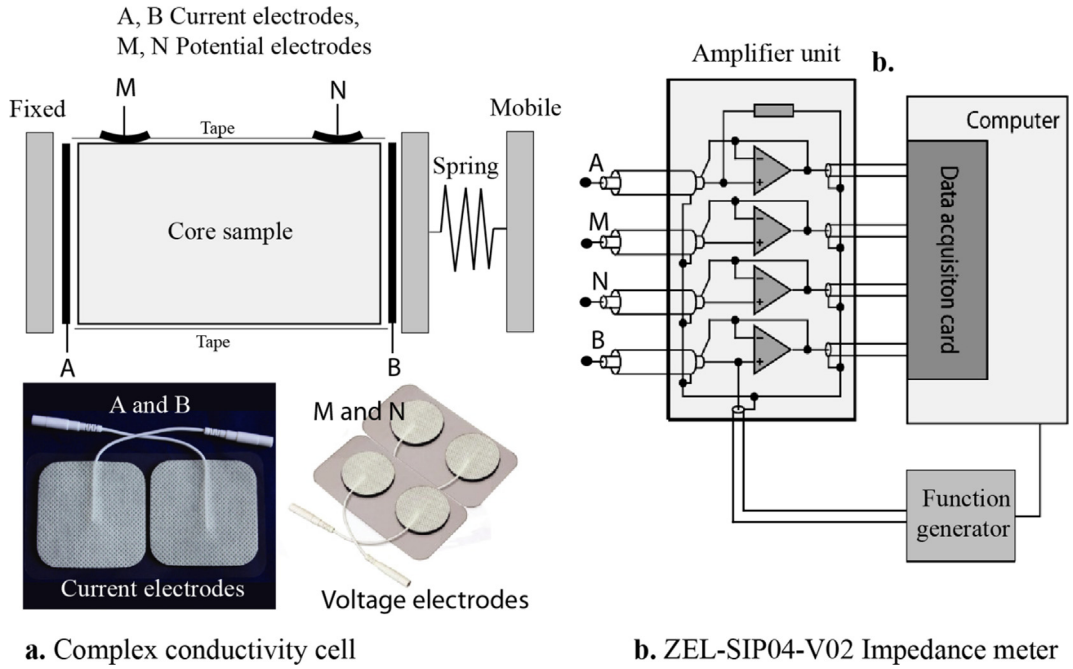

a. Complex conductivity cell **b.** ZEL-SIP04-V02 Impedance meter

Fig. 5. Impedance meter used for the complex (frequency-domain) conductivity spectra for the core samples investigated in this study. **a.** Sketch of the setup showing the position of the current electrodes A and B and the voltage electrodes M and N. The electrodes are self-adhesive super conductive carbon film with a biocompatible hydrogel. **b.** ZEL-SIP04-V02 impedance meter (see Zimmermann et al., 2008, for details). This impedance meter works in the frequency range 1 mHz-45 kHz. The data shown in this study are realized in the frequency range 10 mHz-45 kHz.

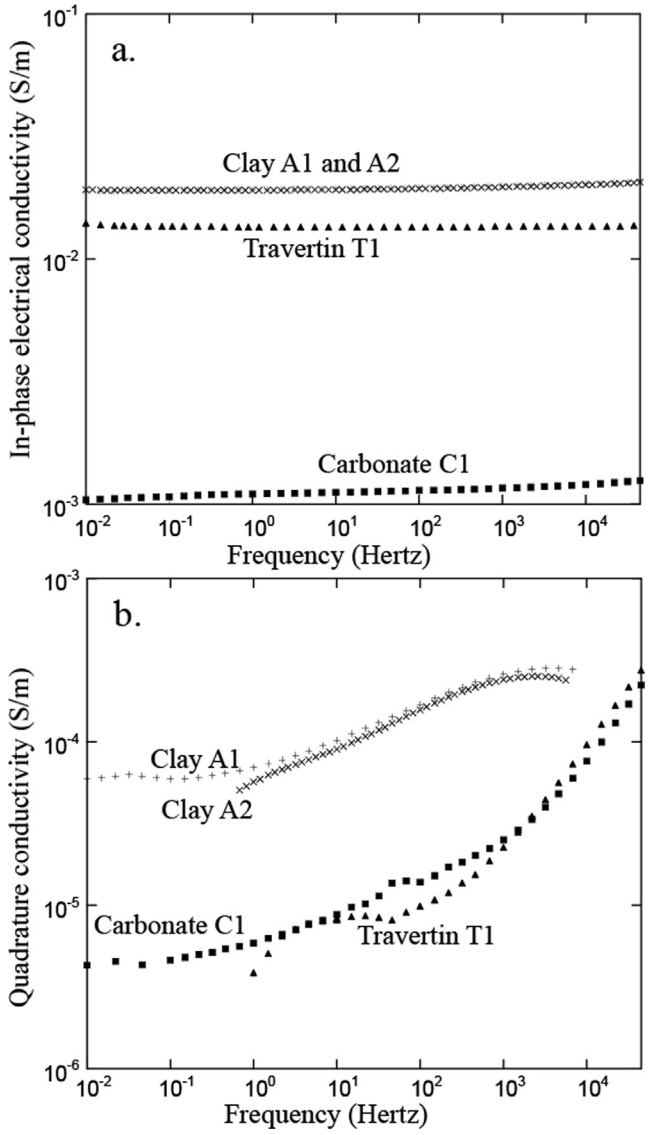

Fig. 6. Complex conductivity spectra. **a.** In-phase conductivity of the four core samples from the test site. **b.** Quadrature conductivity of the four core samples from the test site. We can see that the conductivity of the travertine is close to the conductivity of the clay samples (because of its very high porosity) while the travertine has a quadrature conductivity that is close to the carbonate rock C1 because of its very low CEC.

$$\theta = \left[\frac{1}{\sigma_w}\left(\sigma_\infty - \frac{M_n}{R}\right)\right]^{1/m} \tag{13}$$

This can be done for each element of the tomogram. Then, in turn, we can use Eq. (7) to image the permeability field.

4. Laboratory experiments

Four samples were cored at the site. The experiments were carried out with spring water equilibrated with the rock (pore water conductivity 0.0388 S m^{-1} at 25 °C and pH = 8.7–8.9). A fifth sample corresponding to a clean carbonate rock was added to the collection of core samples to get the induced polarization properties of the unweathered carbonate rock. The porosity of the core samples was estimated with weight and volume measurements. The cation exchange capacity was obtained with the cobalthexamine titration method (Ciesielski et al., 1997). The CEC of the clay sample C1 is 7.2 meq/100 g while the CEC of the travertin is 0.9 meq/100 g and we obtained 0.3 meq/100 g for the limestone.

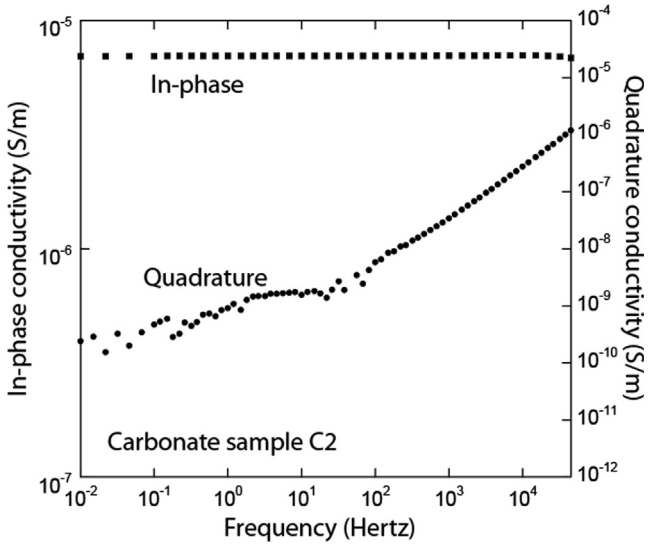

Fig. 7. Complex conductivity spectra for the clean carbonate rock sample C2. Note the very low conductivity and quadrature conductivity.

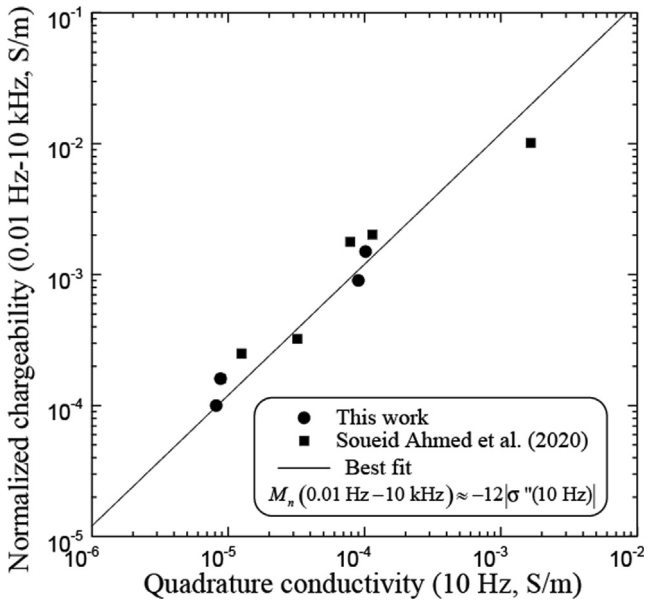

Fig. 8. Normalized chargeability versus quadrature conductivity. The normalized chargeability is determined between a very low frequency (0.01 Hertz) and a high frequency (10 kHz). The quadrature conductivity is determined at the geometric mean frequency of 10 Hertz. The red plain line corresponds to the best fit used to determine the value of $\alpha = 12 \pm 4$. The coefficient α should be equal to 9, which is fairly close to the coefficient determined by fitting. The samples used by Soueid Ahmed et al. (2020) are carbonates rocks.

Frequency-domain induced polarization measurements were performed over the frequency range from 10 mHz to 45 kHz using the ZELSIP04-V02 impedance meter (Zimmermann et al., 2008; see Fig. 5). The complex conductivity spectra are shown in Figs. 6 and 7. The clayey materials are more conductive and polarizable than the carbonate rocks. The clean carbonate rock sample C2 is characterized by very low conductivity and normalized chargeability values. Because of its porosity, the travertine rock sample is quite conductive and it is characterized by a relative low polarization.

Fig. 8 shows the normalized chargeability versus the quadrature conductivity. According to Eq. (8), these two parameters are proportional to each other in agreement with the results shown in Fig. 8. In

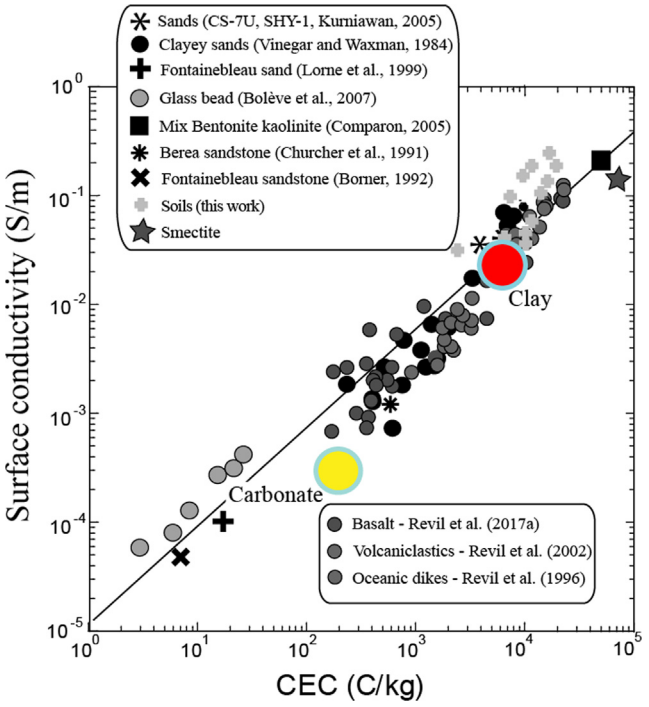

Fig. 9. Surface conductivity versus cation exchange capacity (CEC). The data from the literature are from Bolève et al. (2007; glass beads, NaCl), Vinegar and Waxman (1984; shaly sands, NaCl), Churcher et al. (1991) (CEC for the Berea sandstone), Lorne et al. (1999; Fontainebleau sand KCl), Kurniawan (2005; clean sand, Sample CS-7U), Börner (1992; sample F3 Fontainebleau sandstone), and Comparon (2005; mixtures of MX80 bentonite and kaolinite). The volcanic rock data are from Revil et al. (1996) and Revil et al. (2002). The red filled circle and the yellow filled circle correspond to the clay and carbonate materials investigated in the present study.

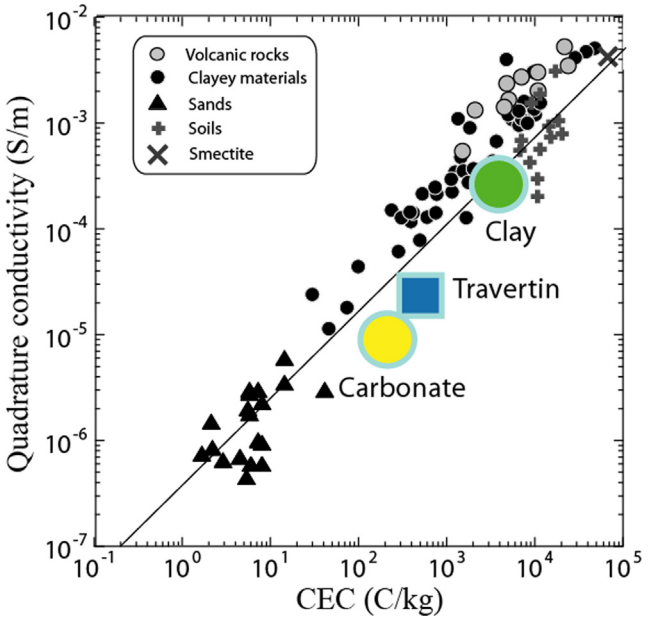

Fig. 10. Quadrature conductivity versus cation exchange capacity (CEC). The black filled symbols shown in the figure are those discussed in Revil et al. (2015). The colored samples are from the present study. Note: 1 meq /(100 g) = 963.2C kg^{-1}. For porous soils and rocks, at full water saturation, the quadrature conductivity is mostly controlled by the cation exchange capacity of the material. The red filled circle and the blue square correspond to the clay and travertine materials, respectively. The yellow filled circle corresponds to the carbonate core sample.

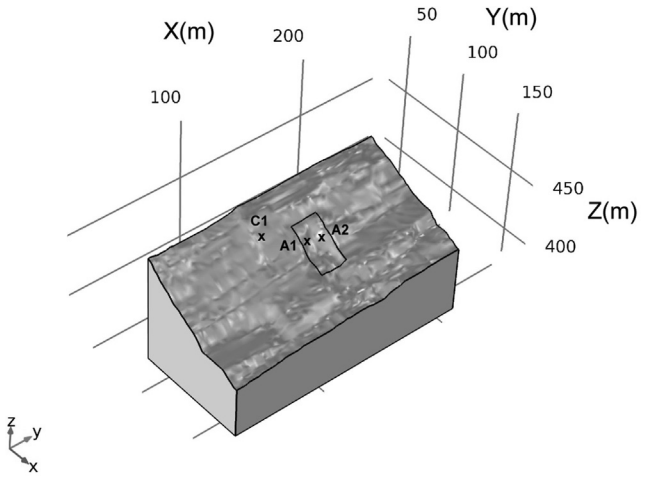

Fig. 11. Topography of the site. The 3D geometry of the site is assembled using a Digital Elevation Model (DEM) describing the topography of the test site. The area delimited by the thin plain line corresponds to the shallow landslide of December 2017. The core sample C1 corresponds to a weathered carbonate rock exposed on a carbonate outcrop. Sample A1 and A2 correspond to plastic clays.

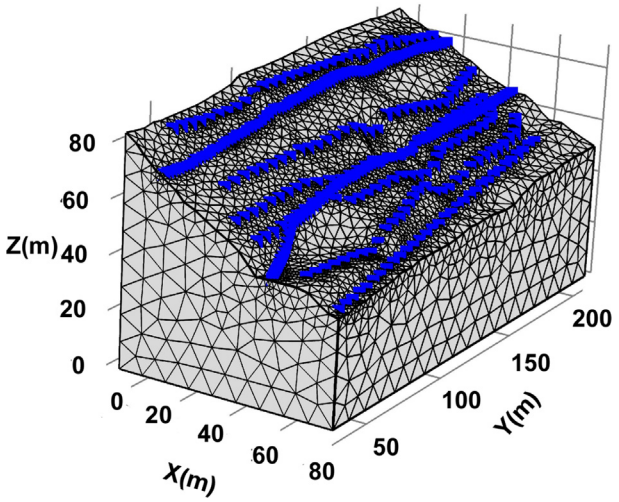

Fig. 12. Simulation domain with the position of the electrodes (blue triangles). This is a 3D representation of the domain of interest meshed with 14,524 finite elements. Eight induced polarization profiles were performed in the field. As shown, the finite element mesh is refined around the electrodes to increase the accuracy of the computations. The profile located at the lowest altitude follows the road shown in Fig. 1. We collected 5971 resistance and 653 apparent chargeability measurements.

Figs. 9 and 10, we compare the dependence of the surface conductivity and quadrature conductivity of our samples on the cation exchange capacity (CEC). We use also data from the literature. The data are consistent with the prediction of Eqs. (3)–(6), which are predicting a linear relationship between the surface conductivity and quadrature conductivity with the CEC. These data confirm that induced polarization measurements in the field should be able to discriminate between clay materials and carbonates. Then, Eqs. (12) and (13) can be used to image the water content and the CEC. This is done in the next section.

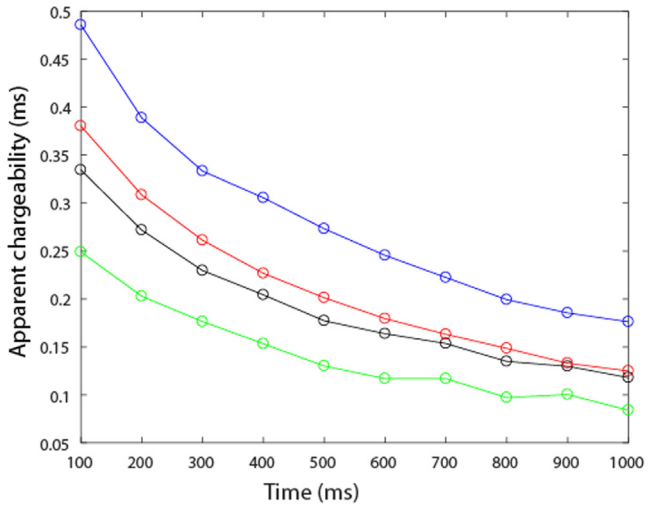

Fig. 13. Decay curves for the secondary voltage in the field time induced polarization data. We observe typical exponential decay curves indicating a good confidence in the raw data.

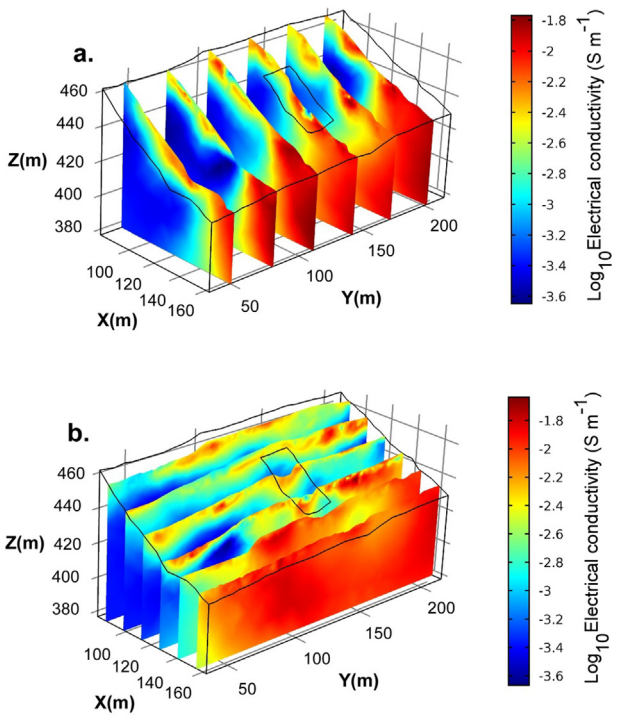

Fig. 14. Electrical conductivity distribution. The conductivity tomogram exhibits mainly two structures. A shallow conductive material corresponding to clays (above 10^{-3} S m^{-1}) and a more resistive layer located beneath the clayey formation, which corresponds to the limestones (with conductivity below 10^{-3} S m^{-1}). The thin closed line corresponds to the landslide area.

5. Field data: Acquisition, interpretation and use of petrophysical models

5.1. Acquisition of the field data

Six induced polarization profiles have been laid out in the field with a length of 165 m (Fig. 1d). The topography is shown in Fig. 11. The topography was built from a Digital Elevation Model (DEM) with a resolution of 1 m (it was difficult to get a better resolution in a woody area). The locations of the 384 electrodes and the mesh are shown in Fig. 12. The mesh was refined around theses electrodes to ensure that

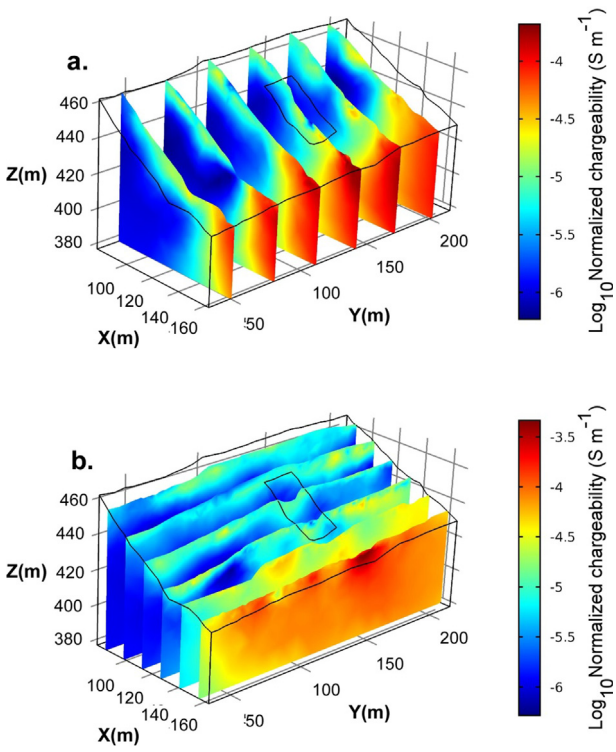

Fig. 15. Normalized chargeability tomography. The normalized chargeability tomogram clearly shows the clays, chargeable (above 10^{-4} S m^{-1}), and the limestones that are less chargeable (below 10^{-5} S m^{-1}). The thin closed line on the top surface corresponds to the landslide area.

the precision of the computations is higher around the points of measurements. We collected 5971 resistance and 653 apparent chargeability measurements with an ABEM SAS4000. The number of resistance data was higher because few longer lines were performed with just resistivity measurements. The simulation domain is discretized into 14,524 elements and the finite element method is used for the forward modeling (Fig. 12). Some examples of decay curves are shown in Fig. 13. We see the good quality of the measurements.

5.2. Tomography

The inversion was performed with the code described in Soueid Ahmed et al. (2018, 2019). We first estimate the conductivity field and then we use it in the estimation the intrinsic chargeability. The convergence of the conductivity and chargeability inversion processes has been obtained after 8 iterations. Fig. 14 shows the estimated electrical conductivity distribution. The conductivity tomograms put in evidence the presence of a conductive anomaly corresponding to clays, below which lies a more resistive carbonate formation. Similarly, Fig. 15 shows the normalized chargeability. Clays are more chargeable than carbonates and are therefore characterized by higher normalized chargeabilities. The plots of the measured and observed data (Fig. 16) show clear linear trends. This means that the computed data match the observed data very well.

5.3. Use of the petrophysical transforms

By using the Eqs. (12) and (13), we can estimate the water content and CEC distributions (see Figs. 17 and 18). As expected, the clays appear to have larger water content due to their high water retention ability. The CEC distribution (see Fig. 18) which is obtained from the water content distribution, associates a higher CEC reaching 3 meq/100 g to the clays close to the value reported in Table 1 (7 meq/100 g).

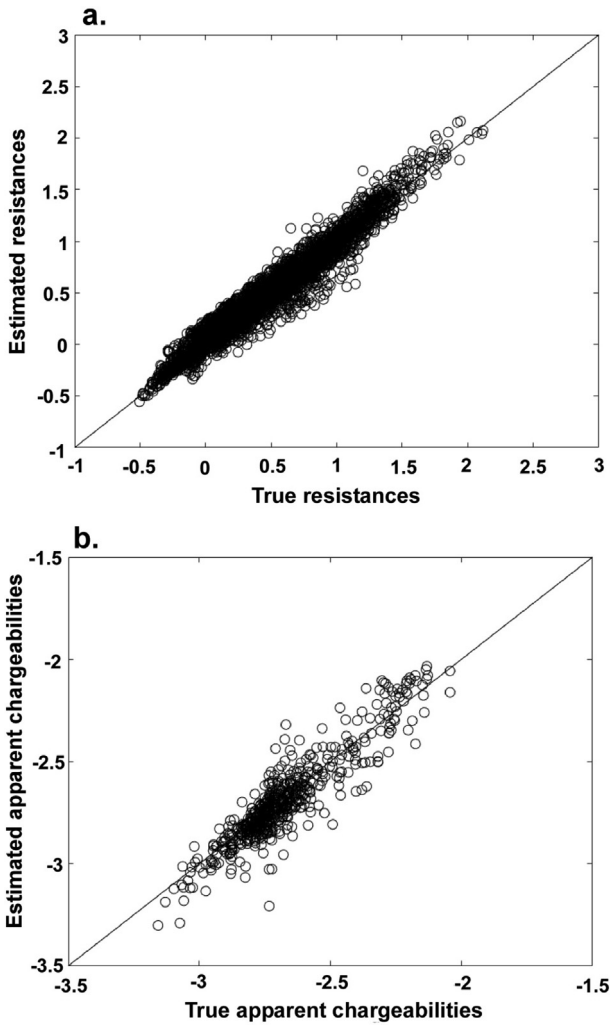

Fig. 16. Result of the inversion. **a.** Resistance data (in Ohm). The scatter plot of the estimated resistances against the true ones shows a linear trend proving that the computed resistances are matching well with the measured ones. **b.** Apparent chargeability data (dimensionless). We plot here the true apparent chargeabilities against the computed ones. The scatter shows the high accuracy in the numerical estimations.

The estimated permeability magnitudes (see Fig. 19) vary between 10^{-18} m^2 and 10^{-13} m^2, which are very reasonable values for such materials (Revil and Cathles, 1999).

5.4. Normalized chargeability versus conductivity

The normalized chargeability versus the conductivity is shown in Fig. 20. We compare here the field data and the laboratory data. There are two poles corresponding to the clay pole and the clean carbonate pole. We see that for the clay pole, the slope of the trend is close to R = 0.10, which means that the conductivity is dominated by the surface conductivity along the surface of the grains. For the clean carbonate, the conductivity is dominated by the conductivity of the pore water.

6. Discussion

We have no information regarding the failure process except that it has been very likely triggered by the heavy rains during the 10 days preceding the event and in particular the day before. The landslide occurs because of a sudden trigger and the clay material liquefied and flow out of the scar damaging the house downslope (retrogression; see e.g., Torrence, 2012, Solberg et al., 2016 for landslides in clayey materials).

The hydrologic and geomorphic interaction between landslides and the drainage network is generally very narrow. The tomograms of the

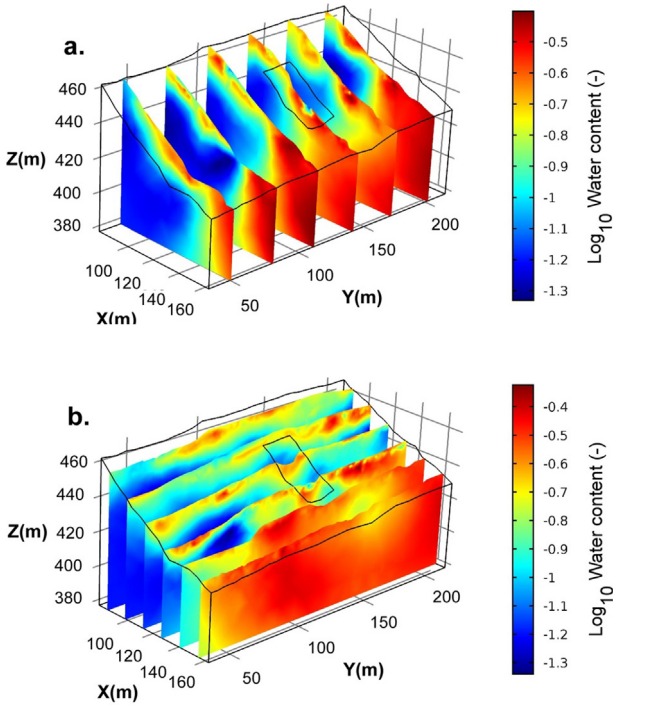

Fig. 17. Water content distribution. The thin closed line corresponds to the landslide area. Note that this area is characterized by the presence of a channel with a high water content.

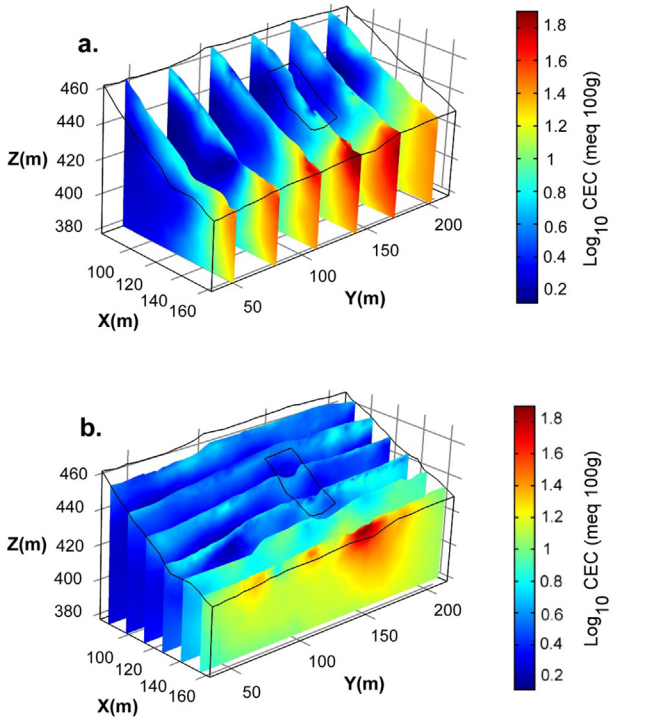

Fig. 18. Cation Exchange Capacity (CEC) distribution. The CEC tomogram exhibits high CEC anomalies corresponding to the presence of plastic clays in the bottom part of the investigated area. The thin closed line corresponds to the landslide area.

Table 1
Physical properties of the four rock samples from the test site. Note: 1 meq /100 g = 963.2C kg^{-1}. The complex conductivity of sample C1 was determined at three salinities to obtain its surface conductivity (0.00029 S m^{-1}). Sample C2 was measured with a pore water conductivity of 0.029 S m^{-1}. The CEC of carbonate C2 was too small to be measured.

Sample	Porosity (−)	CEC (meq/100 g)	Type
A1	0.64	7.2	Clay
A2	0.23	7.2	Clay
T1	0.51	0.9	Travertin
C1	0.14	0.3	Limestone
C2	0.13	-	Limestone

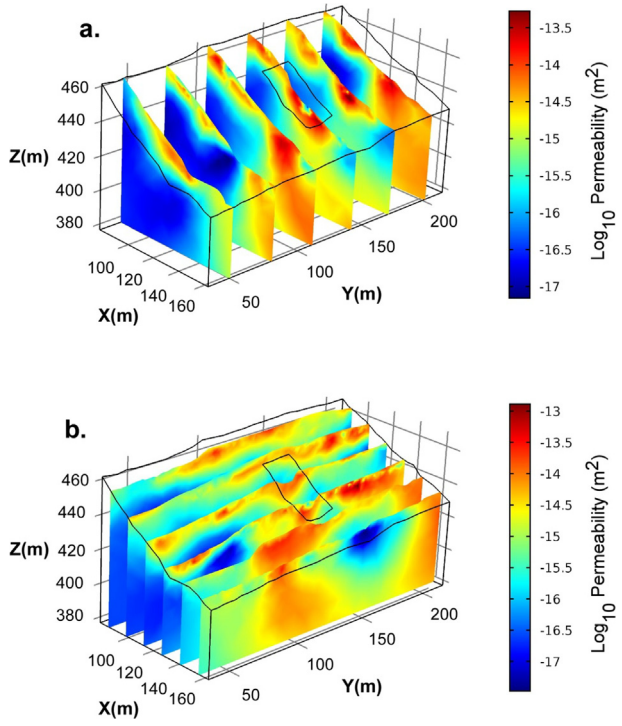

Fig. 19. Permeability distribution. The estimated permeability tomogram represents the clays with high permeability and the carbonates with lower permeability. This is because clays have a high water retention capability. The thin closed line corresponds to the landslide area. Note that the landslide area corresponds to a high permeability flow path channeling water along the slope of the mountain.

permeability and water content show that the landslide is located on a preferential flow path with a clay permeability barrier downslope. At Claix, the stratigraphy thus controlled the relative permeability as well as the pore pressures while water flowing from the path could exert a flow force (Fig. 21). The water saturated conditions may have favored deformation accompanying the initiation of the failure and causing microstructural collapse (Sidle et al., 2006; Picarelli et al., 2012). It could have also generated pore water pressure – varying significantly over a period of hours during heavy rainfall due to direct infiltration and surface flow onto the slope – that facilitated rapid undrained progress of the failure (Salciarini et al., 2006; Tsai et al., 2008) not countered by a stop effect of the materials downstream due to the presence of the road cutting the slope. The picture shown in Fig. 22 corroborates it, indicating the existence of a small karstic conduit in the position of the landslide. We can make the assumption that the karstic conduit formed in the travertine has generated water/pore pressure under/into the rock mass that initiated the collapse as sketched in Fig. 21. This would have quickly generated an overpressure allowing the shallow earth materials to slide easily downslope.

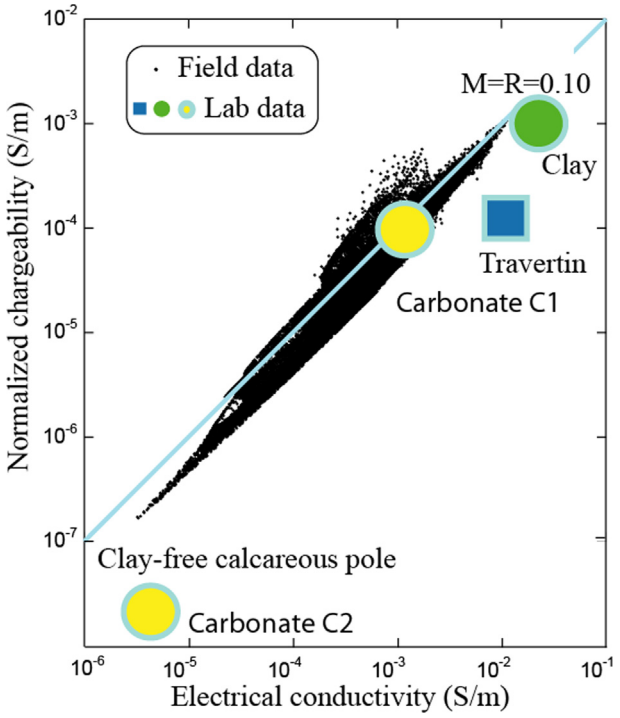

Fig. 20. Normalized chargeability versus electrical conductivity for the field and laboratory data. The ratio between the two parameters corresponds to the chargeability M, which cannot exceed the value of the dimensionless parameter R = 0.10 (independent of the water content, CEC, and temperature).

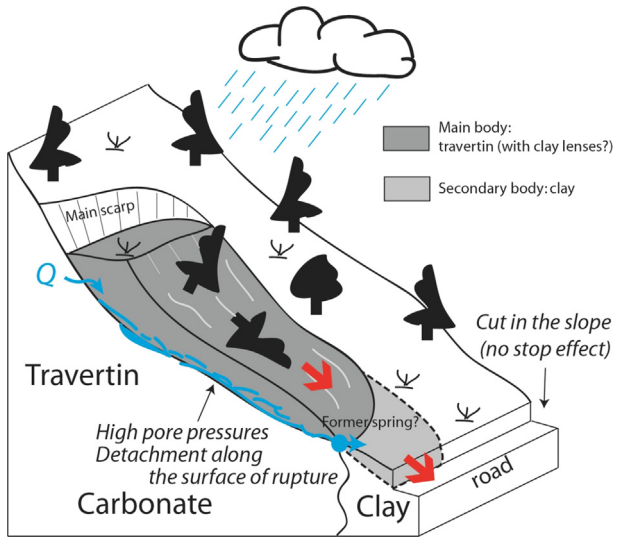

Fig. 21. Sketch of the landslide with the position of the karstic flow pipe with Q the flowrate. The flow pressurizes the rock mass while the pore pressures rise, initiating the landslide which then drives the clay.

7. Conclusions

We investigated the value of induced polarization as a non-intrusive auscultation technique to characterize shallow Earth materials. An application was made on the slope of a woody slope characterized by shallow landslides (a few decimeters to a few meters thick). We first carried out a petrophysical study using four samples from the test site plus a fifth sample corresponding to a clean carbonate rock similar to the carbonate bedrock known to be present at the site. These petrophysical measurements were consistent with a recent mechanistic model called the dynamic Stern layer model and used to provide a

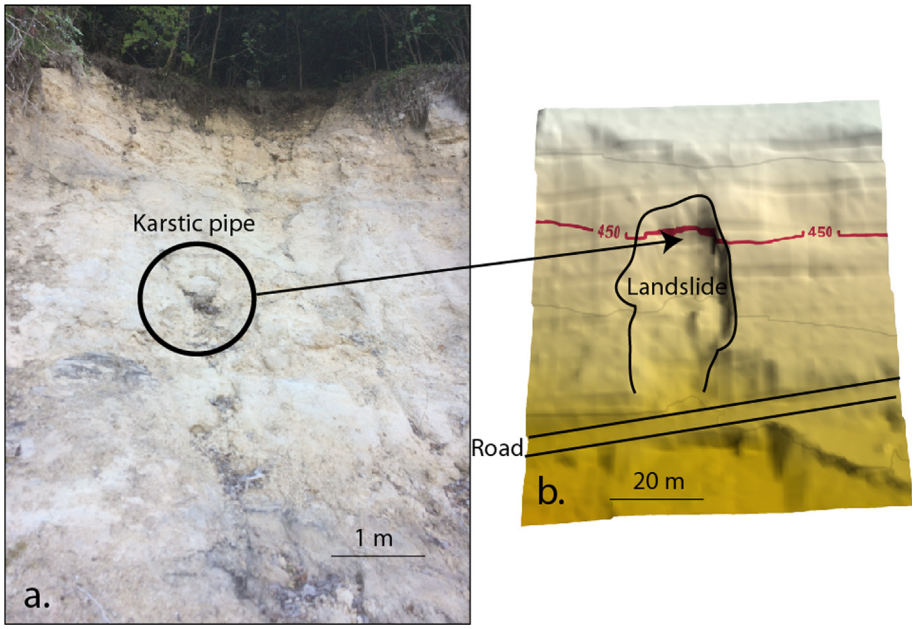

Fig. 22. Picture showing a flow pipe at the base of the decollement zone of the landslide. **a.** Picture of the karstic flow pipe. **b.** Topography of the landslide.

fundamental mechanistic understanding of induced polarization. Then, we applied this petrophysical model to interpret the conductivity and normalized chargeability tomograms obtained in the field using time-domain induced polarization. We developed a procedure to image the water content, the cation exchange capacity, and the permeability distribution at the test site. The cation exchange capacity tomogram provides an image of the 3D repartition of the clay in the field. The permeability field shows that the landslide is associated with a high permeability channel that could have triggered the landslide during an episode of intense rain. These distributions provide some clue regarding the reasons associated with the localization of the landslide. A flow pipe has been identified on the exposed material in the scarp let by the landslide.

As the societal landslide risk will probably increase in the future partly due to the forecast climatic change that may increase the incidence of landslides in many areas, geophysics will undoubtedly have a growing place as a tool to understand and diagnose triggering processes. High permeability flow path that are channeling ground water can for example be highlighted.

CRediT authorship contribution statement

A. Revil: Methodology, Writing - original draft, Writing - review & editing, Data curation, Supervision. **A. Soueid Ahmed:** Methodology, Writing - original draft, Writing - review & editing. **A. Coperey:** . **L. Ravanel:** Writing - review & editing. **R. Sharma:** Writing - review & editing, Writing - review & editing. **N. Panwar:** Writing - review & editing.

Declaration of Competing Interest

The authors declare that they have no known competing financial interests or personal relationships that could have appeared to influence the work reported in this paper.

Acknowledgements

We thank I-RISK (Research, Development and Innovation platform), the region Auvergne Rhône Alpes (France), and the European FEDER fund for their contribution to this study for their contribution to this study. We thank J. Cardon and F. Abdulsamad for their help in the field. We thank the Editor, Jiri Simunek, and the two referees for the quality and speed of the review process.

References

Alpert, P., Ben-Gai, T., Baharad, A., Benjamini, Y., Yekutieli, D., Colacino, M., Diodato, L., Ramis, C., Homar, V., Romero, R., et al., 2002. The paradoxical increase of mediterranean extreme daily rainfall in spite of decrease in total values. Geophys. Res. Lett. 29 (11).

Bertran, P., 2003. The rock-avalanche of February 1995 at Claix (French Alps). Geomorphology 54 (3–4), 339–346. https://doi.org/10.1016/S0169-555X(03)00041-2.

Brückl, E., Brunner, F.K., Lang, E., Mertl, S., Müller, M., Stary, U., 2013. The Gradenbach observatory—monitoring deep-seated gravitational slope deformation by geodetic, hydrological, and seismological methods. Landslides 10, 815–829.

Binley, A., Hubbard, S.S., Huisman, J.A., Revil, A., Robinson, D.A., Singha, K., Slater, L.D., 2015. The emergence of hydrogeophysics for improved understanding of subsurface processes over multiple scales. Water Resourc. Res. 51, 3837–3866. https://doi.org/10.1002/2015WR017016.

Ciesielski, H., Sterckeman, T., Santerne, M., Willery, J.P., 1997. Determination of cation exchange capacity and exchangeable cations in soils by means of cobalt hexamine trichloride. effects of experimental conditions. Agronomie 17 (1), 1–7. https://doi.org/10.1051/agro:19970101.

Götz, A., Zimmermann, M., 1993. The 1991 rock slides in Randa: Causes and consequences. Landslide News 7, 22–25.

Hibert, C., Grandjean, G., Bitri, A., Travelletti, J., Malet, J.P., 2012. Characterizing landslides through geophysical data fusion: Example of the La Valette landslide (France). Eng. Geol. 128, 23–29.

Loew S., Gischig V., Willenberg H., Alpiger A, Moore J.R., 2012. 24. Randa. Edited by John J. Clague, Simon Fraser University, British Columbia, Douglas Stead, Simon Fraser University, British Columbia, Publisher: Cambridge University Press, pp 297-309. https://doi.org/10.1017/CBO9780511740367.025.

Lourenço, S.D.N., Sassa, K., Fukuoka, H., 2006. Failure process and hydrologic response of a two layer physical model: implications for rainfall-induced landslides. Geomorphology 73 (1–2), 115–130.

Lu, N., Godt, J.W., 2013. Hillslope Hydrology and Stability. Cambridge University Press, New York, USA.

Marescot, L., Monnet, R., Chapellier, D., 2008. Resistivity and induced polarization surveys for slope instability studies in the Swiss Alps. Eng. Geol. 98 (1), 18–28.

Maraun, D., Wetterhall, F., Ireson, A.M., Chandler, R.E., Kendon, E.J., Widmann, M., Brienen, S., Rust, H.W., Sauter, T., Themeßl, M., Venema, V.K.C., Chun, K.P., Goodes, C.M., Jones, R.G., Onof, C., Vrac, M., Thiele-Eich, I., 2010. Precipitation downscaling under climate change: Recent developments to bridge the gap between dynamical models and the end user. Rev. Geophys. 48 (3), RG3003.

Malehmir, A., Bastani, M., Krawczyk, C.M., Gurk, M., Ismail, N., Polom, U., Perss, L., 2013. Geophysical assessment and geotechnical investigation of quick-clay landslides – A Swedish case study. Near Surface Geophys. 11 (3), 341–352. https://doi.org/10.3997/1873-0604.2013010.

Malet, J.-P., Durand, Y., Remaître, A., Maquaire, O., Etchevers, P., Guyomarch', G., Déqué, M., van Beek, L.P.H., 2007. Assessing the influence of climate change on the

activity of landslides in the Ubaye Valley. In: McInnes, R., Jakeways, J., Fairbank, H., Mathie, E. (Eds.), Proceedings International Conference on Landslides and Climate Change – Challenges and Solutions. Taylor & Francis, London, pp. 195–205.
Oh, S., Lu, N., 2015. Slope stability analysis under unsaturated conditions: Case studies of rainfall-induced failure of cut slopes. Eng. Geol. 184, 96–103.
Picarelli L., Leroueil S., Olivares L., Pagano L., Tommasi P., Urciulo G., 2012. Groundwater in spodes. In: Clague J.J. and Stead D. (Ed.). Landslides. Types, mechanism and modelling. Cambridge University Press, pp.235-251.
Revil, A., Cathles, L.M., 1999. Permeability of shaly sands. Water Resour. Res. 35 (3), 651–662.
Revil, A., Florsch, N., 2010. Determination of permeability from spectral induced polarization data in granular media. Geophys. J. Int. 181, 1480–1498. https://doi.org/10.1111/j.1365-246X.2010.04573.x.
Revil, A., Coperey, A., Shao, Z., Florsch, F., Fabricius, L.I., Deng, Y., Delsman, J.R., 2017a. Complex conductivity of soils. Water Resourc. Res. 53 (8), 7121–7147. https://doi.org/10.1002/2017WR020655.
Revil, A., Le Breton, M., Niu, Q., Wallin, E., Haskins, E., Thomas, D.M., 2017b. Induced polarization of volcanic rocks. 1. Surface versus quadrature conductivity. Geophys. J. Int. 208, 826–844. https://doi.org/10.1093/gji/ggw444.
Revil, A., Le Breton, M., Niu, Q., Wallin, E., Haskins, E., Thomas, D.M., 2017c. Induced polarization of volcanic rocks. 2. Influence of pore size and permeability. Geophys. J. Int. 208, 814–825. https://doi.org/10.1093/gji/ggw382.
Salvati, P., Petrucci, O., Rossi, M., Bianchi, C., Pasqua, A.A., Guzzetti, F., 2018. Gender, age and circumstances analysis of flood and landslide fatalities in Italy. Sci. Total Environ. 610–611, 867–879. https://doi.org/10.1016/j.scitotenv.2017.08.064.
Salciarini, D., Godt, J.W., Savage, W.Z., et al., 2006. Modeling regional initiation of rainfall-induced shallow landslides in the eastern Umbria Region of central Italy. Landslides 3, 181. https://doi.org/10.1007/s10346-006-0037-0.
Samyn, K., Travelletti, J., Bitri, A., Grandjean, G., Malet, J.-P., 2012. Characterization of a landslide geometry using 3D seismic refraction traveltime tomography: The La Valette landslide case history. J. Appl. Geophys. 86, 120–132.
Sastry, R.G., Mondal, S.K., 2012. Geophysical characterization of the Salna Sinking Zone, Garhwal Himalaya. India. Surv. Geophys. 1–31.
Schmutz, M., Guérin, R., Andrieux, P., Maquaire, O., 2009. Three dimensional internal earthflow structure determination by geophysical means. J. Appl. Geophys. https://doi.org/10.1016/j.jappgeo.2008.12.004.
Schmutz, M., Albouy, Y., Guérin, R., Maquaire, O., Vassal, J., Schott, J., Descloitres, M., 2000. Joint inversion applied to the Super Sauze earthflow (France). Surveys Geophys. 21 (4), 371–390.
Sidle, R.C., OchiaiBook,, H., 2006. Landslides: Processes, Prediction, and Land Use Volume 18. https://doi.org/10.1029/WM018.
Solberg, I.L., Long, M., Baranwal, V.C., Samstadn, A., GyllandJ.S.,, Rønning, 2016. Geophysical and geotechnical studies of geology and sediment properties at a quick-clay landslide site at Esp, Trondheim, Norway. Eng. Geol. 208, 214–230. https://doi.org/10.1016/j.enggeo.2016.04.031.
Soueid Ahmed, A., Jardani, A., Revil, A., Dupont, J.P., 2014. Hydraulic conductivity field characterization from the joint inversion of hydraulic heads and self-potential data. Water Resour. Res. 50 (4), 3502–3522. https://doi.org/10.1002/2013WR014645.
Soueid, Ahmed A., Revil, A., Byrdina, S., Coperey, A., Gailler, L., Grobbe, N., Viveiros, F., Silva, C., Jougnot, D., Ghorbani, A., Hogg, C., Kiyan, D., Rath, V., Heap, M.J., Grandis, H., Humaida, H., 2018. 3D electrical conductivity tomography of volcanoes. J. Volcanol. Geothermal Res. 356, 243–263. https://doi.org/10.1016/j.jvolgeores.2018.03.017.
Soueid Ahmed, A., Revil, A., Gross, L., 2019. Multiscale induced polarization tomography in hydrogeophysics: A new approach. Adv. Water Resourc. 134, 103451. https://doi.org/10.1016/j.advwatres.2019.103451.
Soueid, Ahmed A., Revil, A., Bolève, A., Steck, B., Vergniault, C., Courivaud, J.R., Jougnot, D., Abbas, M., 2020a. Determination of the permeability of seepage flow paths in dams from self-potential measurements. Eng. Geol. 268, 105514. https://doi.org/10.1016/j.enggeo.2020.105514.
Soueid, Ahmed A., Revil, A., Abdulsamad, F., Steck, B., Vergniault, C., Guihard, V., 2020b. Induced polarization as a tool to non-intrusively characterize embankment hydraulic properties. Eng. Geol. 271, 105604. https://doi.org/10.1016/j.enggeo.2020.105604.
Sultana, N., 2020. Analysis of landslide-induced fatalities and injuries in Bangladesh: 2000–2018. Cogent Social Sci. 6 (1), 1737402.
Take, W.A., Bolton, M.D., Wong, P.C.P., Yeung, F.J., 2004. Evaluation of landslide triggering mechanisms in model fill slopes. Landslides 1 (3), 173–184.
Titov, K., Komarov, V., Tarasov, V., Levitski, A., 2002. Theoretical and experimental study of time-domain induced polarization in water saturated sands. J. Appl. Geophys. 50, 417–433.
Titov, K., Tarasov, A., Ilyn, Y., Seleznev, N., Boyd, A., 2010. Relationships between induced polarization relaxation time and hydraulic properties of sandstone. Geophys. J. Int. 180, 1095–1106. https://doi.org/10.1111/j.1365-246X.2009.04465.x.
Torrence J.K., 2012. Landslides in quick clay. In: Clague J.J. and Stead D. (Ed.). Landslides. Types, mechanism and modelling. Cambridge University Press, pp. 83-94.
Tsai, T.-L., Chen, H.-E., Yang, J.-C., 2008. Numerical modeling of rainstorm-induced shallow landslides in saturated and unsaturated soils. Environ. Geol. 55, 1269–1277. https://doi.org/10.1007/s00254-007-1075-1.
Vinegar, H., Waxman, M., 1984. Induced polarization of shaly sands. Geophysics 49 (8), 1267–1287. https://doi.org/10.1190/1.1441755.
Weller, A., Slater, L., Binley, A., Nordsiek, S., Xu, S., 2015. Permeability prediction based on induced polarization: Insights from measurements non sandstone and unconsolidated samples spanning a wide permeability range. Geophysics 80 (2), D161–D173.
Yang, Z., Cai, H., Shao, W., et al., 2019. Clarifying the hydrological mechanisms and thresholds for rainfall-induced landslide: In situ monitoring of big data to unsaturated slope stability analysis. Bullet. Eng. Geol. Environ. 78 (4), 2139–2150.
Zimmermann, E., Kemna, A., Berwix, J., Glaas, W., Münch, H.M., Huisman, J.A., 2008. A high-accuracy impedance spectrometer for measuring sediments with low polarizability. Measure. Sci. Technol. 19 (10), 105603. https://doi.org/10.1088/0957-0233/19/10/105603.